



Substrate-mediated leg interactions play a key role in insect stability on granular slopesMiguel Piñeirua ^{*}, Anna Verbe , and Jérôme Casas*Institut de Recherche sur la Biologie de l'Insecte, Université François Rabelais, 37000 Tours, France*

(Received 21 April 2023; accepted 26 May 2023; published 25 July 2023)

Locomotion on granular inclines is a subject of high relevance in ecological physics as well as in biomimetics and robotics. Enhancing stability on granular materials represents a huge challenge due to the fluidization transition when inclination approaches the avalanche angle. Our motivating example is the predator-prey system made of the antlion, its pit, and its prey. Recent studies have demonstrated that stability on granular inclines strongly depends on the pressure exerted on the substrate. In this work we show that for multilegged locomotion, along with pressure, the distance between the leg contacts on the substrate also plays a major role in the determination of the stability threshold. Through a set of model experiments using artificial sliders, we determine a critical distance below which stability is importantly affected by the interactions between the perturbed regions generated by each contact point. A simple model based on the Coulomb method of wedges allows us to estimate a stability criterion based on pressure, interleg distance, and substrate characteristics. Our work suggests that mass to leg-length allometric relationships, as the ones observed in ants, may be an important key in determining the locomotion success of multilegged locomotion on granular inclines.

DOI: [10.1103/PhysRevE.108.014903](https://doi.org/10.1103/PhysRevE.108.014903)**I. INTRODUCTION**

Ubiquitous in nature, locomotion in granular media has drawn the attention of the scientific community in recent years [1–3]. Because of their complex nature [4], interactions with granular materials offer a rich field of study. In nature, solid-fluid transitions in granular media are masterly exploited by the antlion larvae in order to catch prey [5–7]; they dig a conical pit into the sand and wait at the bottom for their victims to fall down. In fact, for most of the antlion's prey, locomotion on the inclined pit walls represents an insurmountable challenge. The antlion builds its pit with an inclination near the avalanche angle, and thus, small perturbations generated by prey at the leg-substrate contact points can generate local deformations, making locomotion almost impossible and, in some cases, causing prey to fall all the way down to the bottom of the trap [8]. The efficiency of the antlion's trap depends on different parameters, including pit architecture, the behavior of antlion larvae, and prey characteristics [9,10]. Moreover, not only prey physical characteristics such as weight and size can play an important role in the capture success of the antlion's pit [10], but prey gate pattern adaptations to locomotion on granular inclines can also be important [11]. Understanding the physical principles determining locomotion stability on granular inclines is thus of high relevance for ecological physics, as well as for biomimetics and robotics [2,12,13].

In a previous work, Crassous *et al.* [14] showed that the stability of an inert disk with density ρ_s and height h lying on a granular slope with density ρ and grain size δ depends on three main parameters: the nondimensional pressure exerted by the object on the substrate $P^* = \rho_s h / \rho \delta$, the inclination

angle difference from the avalanche $\Delta\theta$, and the object area in contact with the substrate Σ . The authors observed that the stability of light objects on the granular incline did not follow the Amonton's law. In the case of very light objects, $P^* \ll 1$, they do not perturb the surface and stability is achieved only by friction between the object and the granular media. In contrast, for heavy objects, $P^* \gg 1$, stability is obtained by the formation of a rim in front of the object due to the large deformation of the media. However, for intermediate objects, $P^* \sim 1$, the pressure exerted on the substrate destabilizes the medium, causing the object to slide down the slope. In the latter case, the object slides despite the formation of a frontal rim. Pressure-dependent stability on granular inclines is of great interest in the study of animal locomotion, and in particular in the case of insects (i.e., ants climbing an antlion's pit), for whom the pressures exerted on the granular media lie at the frontier between this unstable region and the stable region defined by the presence of rims. An important aspect in the walking stability of multilegged animals on granular slopes is the interaction between the rims generated by each one of the leg contacts on the granular. The existence of rim interactions due to the proximity of contact points could potentially modify the animal's stability. In the present work we address this problem by studying the influence of rim interactions on the static stability of multilegged artificial objects on inclined granular planes. We focus on the influence of the different parameters that are relevant in ecological settings: the pressure exerted on the substrate, the interleg distance, and the grain size.

II. MATERIALS AND METHODS

Experiments are carried out using a box of dimensions $30 \times 30 \times 3.5$ cm (width-length-height) in which we pour

*miguel.pineirua@univ-tours.fr

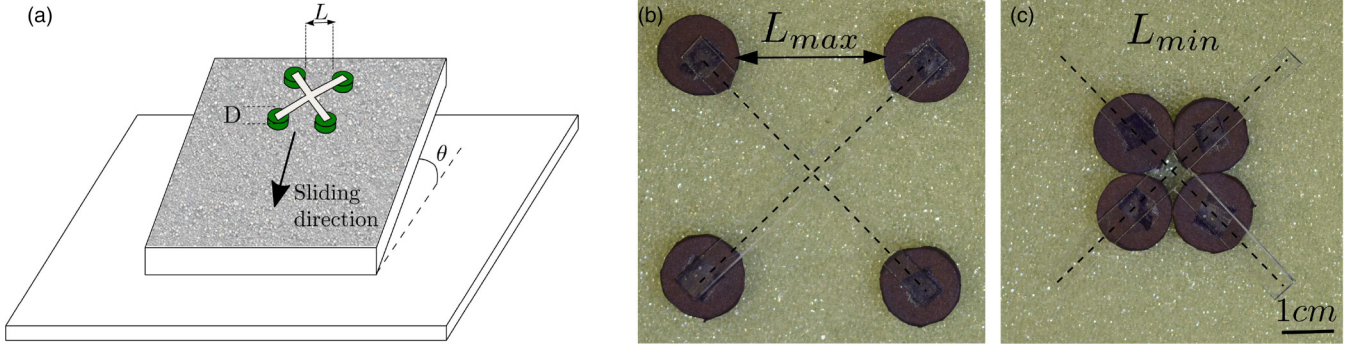


FIG. 1. (a) Scheme of the experimental device. (b) and (c) Image of the artificial slider in its extreme configurations of maximum and minimum values of L , respectively. Dashed lines are a guide to the eye to identify the plexiglass structure joining the four plexiglass disks.

glass beads of different diameters ($\delta = 0.5, 1, \text{ and } 2 \text{ mm}$) and density $\rho = 2500 \text{ kg/m}^3$. Once the box is fully filled with granular beads, we use a ruler to take away the excess of beads in order to obtain a regular flat surface. The final granular preparation presents a solid volume fraction of $\varphi = 0.6 \pm 0.05$ with a mean avalanche angle of $\theta_a = 28.3^\circ \pm 0.8^\circ$ for the $\delta = 0.5 \text{ mm}$ beads, $\theta_a = 26.2^\circ \pm 0.5^\circ$ for the $\delta = 1 \text{ mm}$ beads, and $\theta_a = 29.2^\circ \pm 0.8^\circ$ for the $\delta = 2 \text{ mm}$ beads. In a typical experiment, after the surface has been flattened, the granular preparation is tilted up to an angle of $\theta < \theta_a$ so that $\Delta\theta = \theta_a - \theta = 3^\circ$. A four-legged artificial slider is then gently put on the granular surface near the top edge of the box [Fig. 1(a)]. The slider consists of four plexiglass disks fixed together through a rigid plexiglass structure. Two different artificial sliders with different disk diameters of $D = 7.5$ and 15 mm are used. The distance between the disks can be varied in order to obtain an interdisk distance in the range $0 < L < 10 \text{ cm}$ (see Fig. 1). Following the work of Crassous *et al.* [14], the mass of the artificial slider is chosen to be such that the exerted pressure is $P^* \sim 2.5$, thus lying near the unstable-stable transition zone. The mass of each slider is adjusted depending on the disk diameter and grain size in order to preserve a constant value of P^* .

In all cases we verify that the thickness of the disks is bigger than the penetration depth into the granular media. The outcome of each experiment is dichotomous: a value of 1 is assigned if the slider falls all the way down the slope reaching the bottom border of the box or 0 if the previous condition is not fulfilled, as in Crassous *et al.* [14]. In general, the artificial slider slips a distance of $\sim D$ before reaching full stability on the granular incline. The sliding probability for each set of interdisk distance L and grain size δ is obtained by repeating each experiment ten times.

III. RESULTS

The sliding probability of the artificial sliders as a function of the nondimensional parameter L/D is shown in Fig. 2. The choice of using D as the typical distance to normalize L will be discussed further. For all grain sizes and disk diameters we observe a transition from the unstable to the stable region as the distance L increases. For very close contacts, such as in Fig. 1(c), the sliding probability is maximal ($p \sim 1$) and starts to decrease as the distance increases. At some critical

distance, the sliding probability reaches a minimum ($p \sim 0$), remaining constant as L is further increased. We observe a good collapse of data when L is normalized by D , independently of the grain size. Our experiments show that stability is reached despite grain size when the distance between the disks is about 2.5 times the diameter of the disk. During experiments with small interdisk distances (small L/D), we could observe grain displacements in the inside of the entire squared region defined by the four disk contacts. That is, the perturbation zone generated by each contact merged with the neighboring perturbations, defining a single perturbation zone. Also, the frontal rims generated by contiguous disks tend to form a unique rim. In contrast, for high values of L/D , the perturbation zones generated by each disk do not interact and independent rims at each disk can be easily identified. The size of the perturbation zone created around each contact point, thus, obviously plays an essential role in the stability of the slider. More precisely, the question is: how does this perturbation distance compare to the interdisk distance L ?

A. Perturbation size

A first postulate is that the extent of the perturbation zone around the contact between each disk and the granular surface

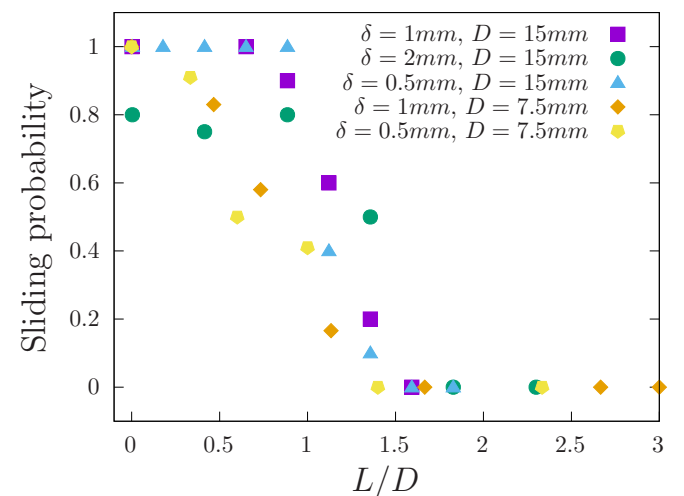


FIG. 2. Sliding probability as a function of the nondimensional parameter L/D . The substrate inclination is fixed to $\Delta\theta = 3^\circ$.

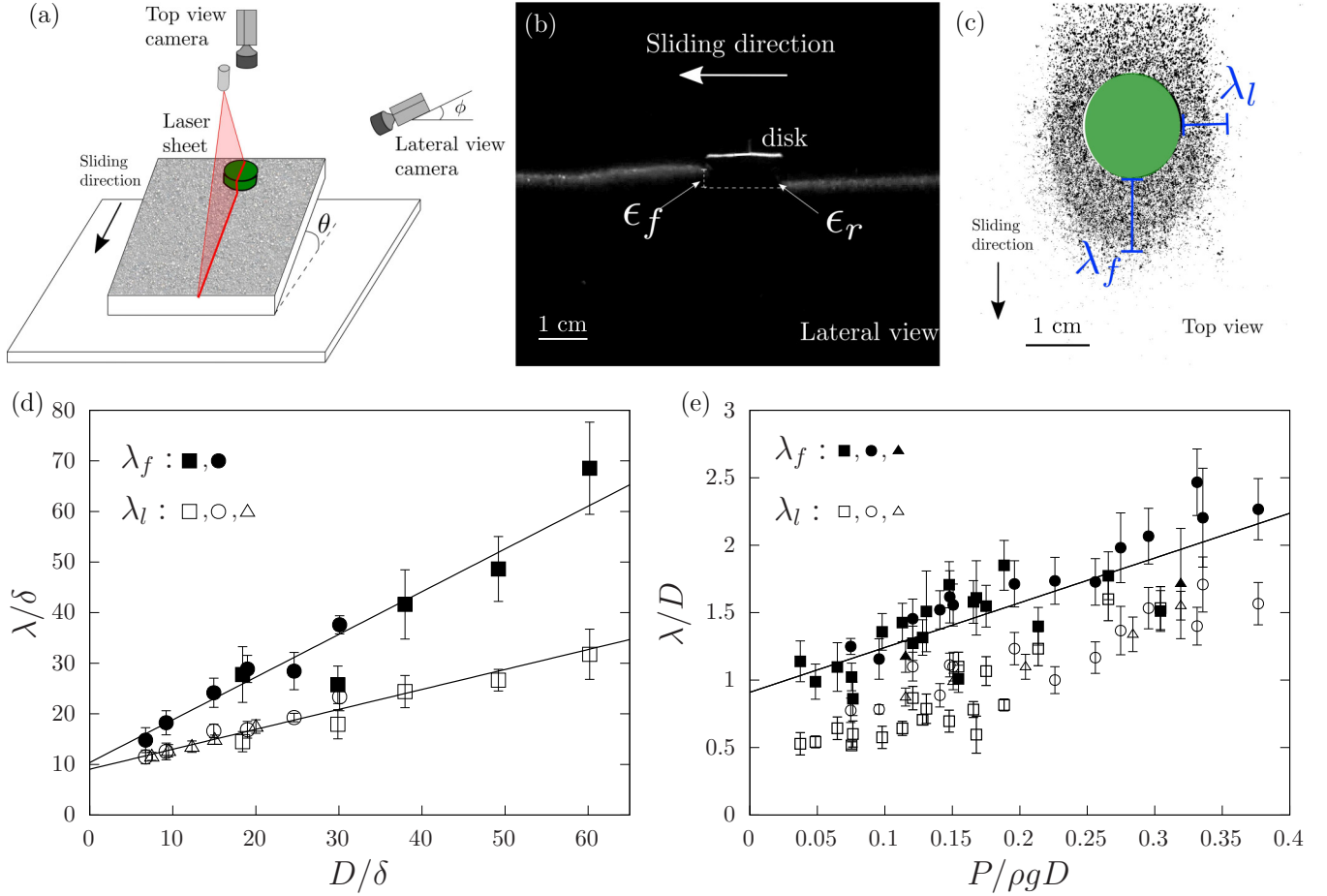


FIG. 3. (a) Schema of the experimental setup used for the estimation of the perturbation distance λ and the rim height ϵ . (b) Lateral view of the disk deforming the granular surface. Only the red channel of the RGB image is shown. The rim height ϵ is obtained from the laser projection on the granular surface. (c) Binarized image of the perturbation extent produced by the sliding disk on the granular bed. The image is obtained from the difference between the top view images before and after the deposition of the disk on the granular surface. (d) Plot of the normalized perturbation lengths λ_f/D (solid points) and λ_l/D (empty points) as a function of the normalized disk diameter D/δ for a constant nondimensional pressure $P^* = 2.5$ and for three different grain sizes: \square , $\delta = 0.5$ mm; \circ , $\delta = 1$ mm; and \triangle , $\delta = 2$ mm. The equations of the linear regressions are $\lambda_f = 0.85D + 10\delta$ and $\lambda_l = 0.4D + 9\delta$. (e) Plot of the normalized perturbation lengths λ_f/D (solid points) and λ_l/D (empty points) as a function of the normalized pressure $P/\rho g D$. The equation of the linear regression is $\lambda_f = 3.45P/\rho g + 0.9D$.

is expected to depend on both the grain size and the disk diameter, as observed in the case of velocity fields of objects into granular media [15]. We can also expect the perturbation size to depend on the pressure exerted by the disk on the granular substrate [16]. To explore these dependencies, we carried out two sets of experiments. In the first one, we placed single circular plexiglass disks of different diameters ($D = 5, 10, 15, 20, 25,$ and 30 mm) on an inclined granular bed ($\Delta\theta = 3^\circ$) composed of the same spherical glass beads of diameters $\delta = 0.5$ mm, $\delta = 1$ mm, and $\delta = 2$ mm used in the slider experiments. The mass of each disk was adjusted in order to keep a constant pressure, $P^* = 2.5$ (the same as in the sliding probability measurements). In the second set of experiments, the disks with diameters $D = 7.5, 15,$ and 30 mm were loaded with additional masses on top in order to generate nondimensional pressures P^* in the range $0.8 < P^* < 5.6$. For both sets of experiments, the perturbation generated on the granular bed was measured by comparing the top view images of the granular surface before and after the deposition of the circular objects [see Figs. 3(a) and 3(b)]. Thus, our

measurements indicate the extent at which glass beads moved from their initial position after the deposition of the disks on the substrate. In the second set of experiments (varying P^*), besides measuring the perturbation extent λ , we also measured the height of the frontal rim ϵ_f generated after deposition of the disks on the granular surface. These measurements were carried out using the classical technique of laser profilometry shown in Figs. 3(a) and 3(c). Our experiments show that the perturbation zone has an ellipselike form defined by a frontal perturbation distance λ_f (measured in the direction of the slope) and a lateral distance λ_l (perpendicular to λ_f). Both distances, λ_f and λ_l , were measured from the border of the disk to the beginning of the region where no more grain movements were observed [see Fig. 3(c)]. In the case of stable disk conditions, λ_f and λ_l correspond to the perturbation lengths at the instant of complete arrest. For nonstable conditions (disks sliding all the way down to the end of the slope), these measurements correspond to the maximum perturbation length observed during the disk displacement. The results of our first set of experiments (varying D and δ with P^* fixed) are

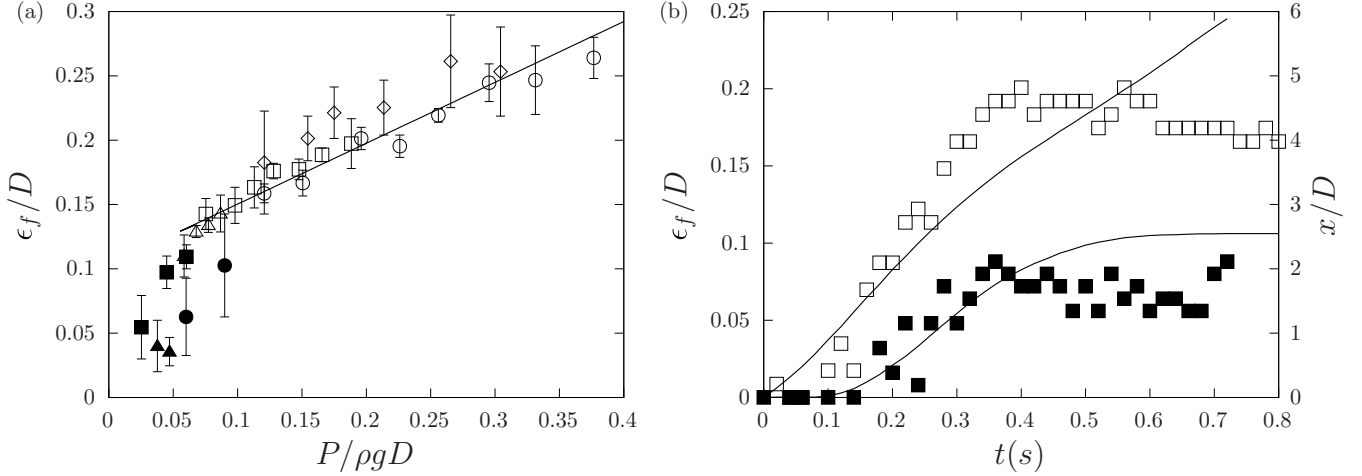


FIG. 4. (a) Nondimensional depth ϵ_f/D as a function of $P/\rho g D$. Symbols represent different experimental conditions: $\square \rightarrow D = 15$ mm and $\delta = 0.5$ mm, $\circ \rightarrow D = 15$ mm and $\delta = 1$ mm, $\triangle \rightarrow D = 30$ mm and $\delta = 1$ mm, and $\diamond \rightarrow D = 7.5$ mm and $\delta = 0.5$ mm. Empty and solid symbols represent arrest and sliding conditions, respectively. The linear regression is calculated only for arrest conditions, $\epsilon_f/D = \beta P/\rho g D + 0.1$, with $\beta = 0.47 \pm 0.02$, and $R^2 = 0.86$. (b) Temporal evolution of the nondimensional depth ϵ_f/D (points) and slider position x/D (lines) for two different pressures: $P^* = 1.35$ (solid points and solid line) and $P^* = 5.4$ (empty points and dashed line).

shown in Fig. 3(d). We observe that the perturbation length in both directions λ_f and λ_l linearly increase with the disk and grain diameters (D and δ , respectively). These results show that the effects of the disk diameter on the frontal perturbation length λ_f start to be dominant for $D/\delta > 10$. The latter may explain the good collapse of the probability curve (Fig. 2) when the interdisk distance L is normalized with respect to D , as the slider experiments lie in the range $7.5 < D/\delta < 30$. We also find a better collapse of data when choosing D as the characteristic length for the variable pressure experiments. In Fig. 3(e) we present the evolution of λ_f/D and λ_l/D as a function of the nondimensional pressure $P/\rho g D$. The choice of $\rho g D$ as characteristic pressure also allows us to integrate the results of our first set of experiments in the plot. Both perturbation lengths λ_f/D and λ_l/D are observed to vary linearly with pressure as $\sigma P/\rho g D$, with $\sigma = 3.45 \pm 0.28$. As for the perturbation extension, the height of the frontal rim also appears to be dependent on pressure [Fig. 4(a)]. After being deposited on the surface, disks start to slide downwards while penetrating into the granular media due to pressure. During this initial displacement, the ploughed material accumulates in front of the disk, generating a rim of height ϵ_f with respect to the bottom of the disk [see Fig. 4(b)]. We observe that for small pressures, the rim height is not enough to keep the disks from sliding down the incline [these cases are represented as solid points in Fig. 4(a), where ϵ_f is taken as the mean height value during the disk motion]. This contrasts with heavier disks [empty points in Fig. 4(a)], which generate a sufficiently high frontal rim to come to a full stop. In the latter case the rim height is measured at the moment of complete arrest. Interestingly, the unstable-stable transition occurs at a rim height of $\epsilon_f/D \sim 0.15$, which corresponds to the nonlinear to linear transition of the relation between penetration depth and force resistance observed in the case of the penetration of solids in granular media [17]. The linear regression of the experimental data for the complete arrest cases [empty points in Figure 4(a)] gives $\epsilon_f/D \sim \beta P/\rho g D$, with $\beta = 0.47 \pm 0.02$.

B. Rim force

A stability criterium for the artificial slider used in our experiments can be found by balancing the component of its weight in the direction tangential to the sliding plane and the force exerted by the rim generated in front of it. In order for the slider to stay still on the incline, the component of its weight tangential to the sliding plane $T = N\pi/4PD^2 \sin \theta$, where N is the number of disks and P is the total pressure, must be lower than the sum of the resistive forces generated at the frontal rims formed at each contact point. Let f_r be the force of an individual rim. Using the Coulomb method of wedges [18], the force exerted by the rim on a single disk can be estimated as

$$f_r = \frac{\rho g \epsilon_f^2}{2} D \cos(\theta) f_{\min}(\mu, \zeta, \kappa), \quad (1)$$

where ϵ_f is the height of the frontal rim, $\mu = \tan \theta_a$, and $\zeta = \tan \theta$. Equation (1) represents the minimal force needed to move a block of volume $V = D\epsilon_f^2(\kappa^2/\tan \Delta\theta + (1 - \kappa)^2/\tan \alpha)/2$ up the sliding plane of inclination α with respect to the undeformed surface [where κ is the proportion of the rim height beneath the level of the undeformed surface, see Fig. 5(a)]. In our experiments, the displaced volume is composed of two parts: the first one corresponds to the volume of ploughed material in front of the disk [hatched region in Fig. 5(a)]. During the initial sliding, the ploughed granular material accumulates, forming a wedge with an angle of $\Delta\theta = \theta_a - \theta$ with respect to the inclined undeformed surface. The height of this upper wedge is $\kappa\epsilon_f$ (a fraction of the total measured rim height ϵ_f , with $0 < \kappa < 1$) and its length is $\kappa\epsilon_f/\tan \Delta\theta$. The second part of the displaced volume is the wedge formed beneath the level of the undeformed surface and defined by the slip plane angle α and the penetration depth of the disk into the granular material $(1 - \kappa)\epsilon_f$. The function f_{\min} in Eq. (1) is obtained by minimization with respect to α (refer to Ref. [18] for a detailed description of

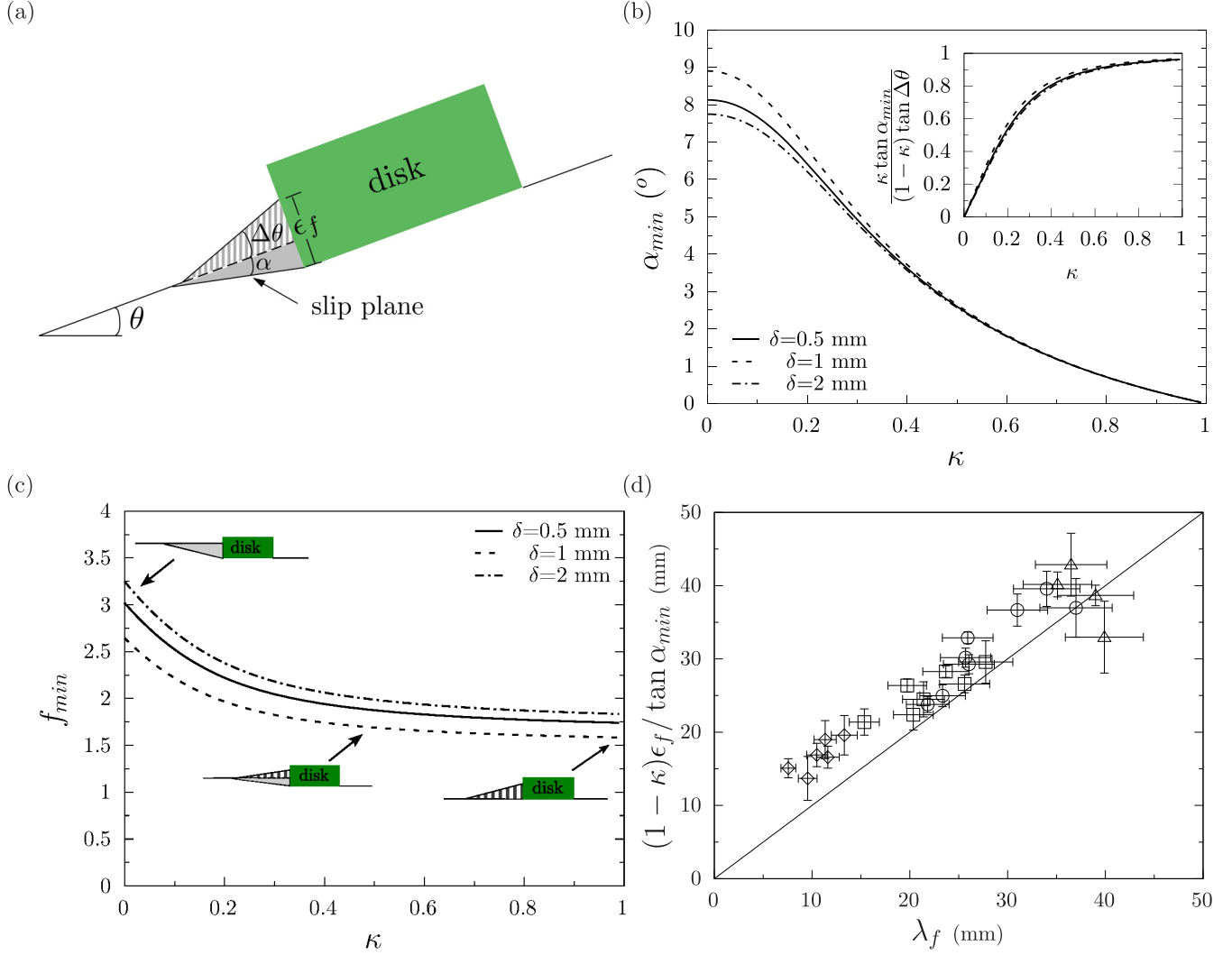


FIG. 5. (a) Structure of the frontal rim. The hatched region over the flat plane corresponds to the ploughed volume during the initial sliding. The wedge lying beneath the surface is defined by the slip plane angle α . (b) Evolution of the slip plane angle α_{\min} as a function of κ for different grain sizes. Each grain size implies a different value of θ_a : for $\delta = 0.5$ mm, $\theta_a = 28^\circ$; for $\delta = 1$ mm, $\theta_a = 26^\circ$; and for $\delta = 2$ mm, $\theta_a = 29^\circ$. In all three cases $\Delta\theta = \theta_a - \theta = 3^\circ$. Inset: Ratio of the upper (hatched) and lower (gray) wedge lengths as a function of the proportion parameter κ . (c) Value of f_{\min} as a function of κ for different grain sizes. (d) Lower wedge length $(1 - \kappa)\epsilon_f / \tan \alpha_{\min}$ compared to λ_f using $\kappa = 0.5$ and $\alpha_{\min} = 2.6^\circ$. Symbols represent different experimental conditions: $\square \rightarrow D = 15$ mm and $\delta = 0.5$ mm, $\circ \rightarrow D = 15$ mm and $\delta = 1$ mm, $\triangle \rightarrow D = 30$ mm and $\delta = 1$ mm, and $\diamond \rightarrow D = 7.5$ mm and $\delta = 0.5$ mm.

the procedure). The values of α minimizing f are presented in Fig. 5(b) as a function of κ . The steepest inclination of the slip plane is obtained when the granular surface beneath is undeformed (i.e., $\kappa = 0$). The presence of ploughed material on top of the surface leads to a reduction of the slip angle α_{\min} as the value of κ increases. This effect was also observed in previous studies [19,20] in the case of a vertical plate dragged through a granular bed. Also in agreement with these works, the Coulomb method of wedges estimation presented here shows that the length of the upper and lower wedges tend to the same value as κ increases [inset in Fig. 5(b)]. Moreover, a decreasing value of the slip plane inclination angle leads to a decrease of f_{\min} [Fig. 5(c)]. In the present work κ is not a controlled parameter but the result of the penetration dynamics of the disks after deposition on the inclined granular surface. In our experiments the measured value of κ remains fairly constant, $\kappa \sim 0.5$, despite the changes of the applied

pressure. For this value of κ we get an estimated value of the slip plane angle of $\alpha_{\min} = 2.6^\circ$. Using these values we can estimate the wedge length as $(1 - \kappa)\epsilon_f / \tan \alpha_{\min}$, which is in good agreement with the perturbation extension λ_f measured throughout our experiments [Fig. 5(d)].

C. Rim interaction

In what follows we assume that for big interdisk distances, i.e., $L/D \gg 1$, the rim force on each one of the disks of the artificial slider is given by Eq. (1). This force can, however, be affected as $L \rightarrow \min\{\lambda_f, \lambda_t\}$, due to the interaction between rims. A simple geometrical approach allows one to determine the total rim force in the two extreme cases presented in Figs. 1(b) and 1(c). In the limit $L \rightarrow 0$ [Fig. 1(c)], the four disks form a compact object of width $2D$, so that the total force on the slider is $F_t = 2f_r$. In contrast, when $L \gg D$ [Fig. 1(b)],

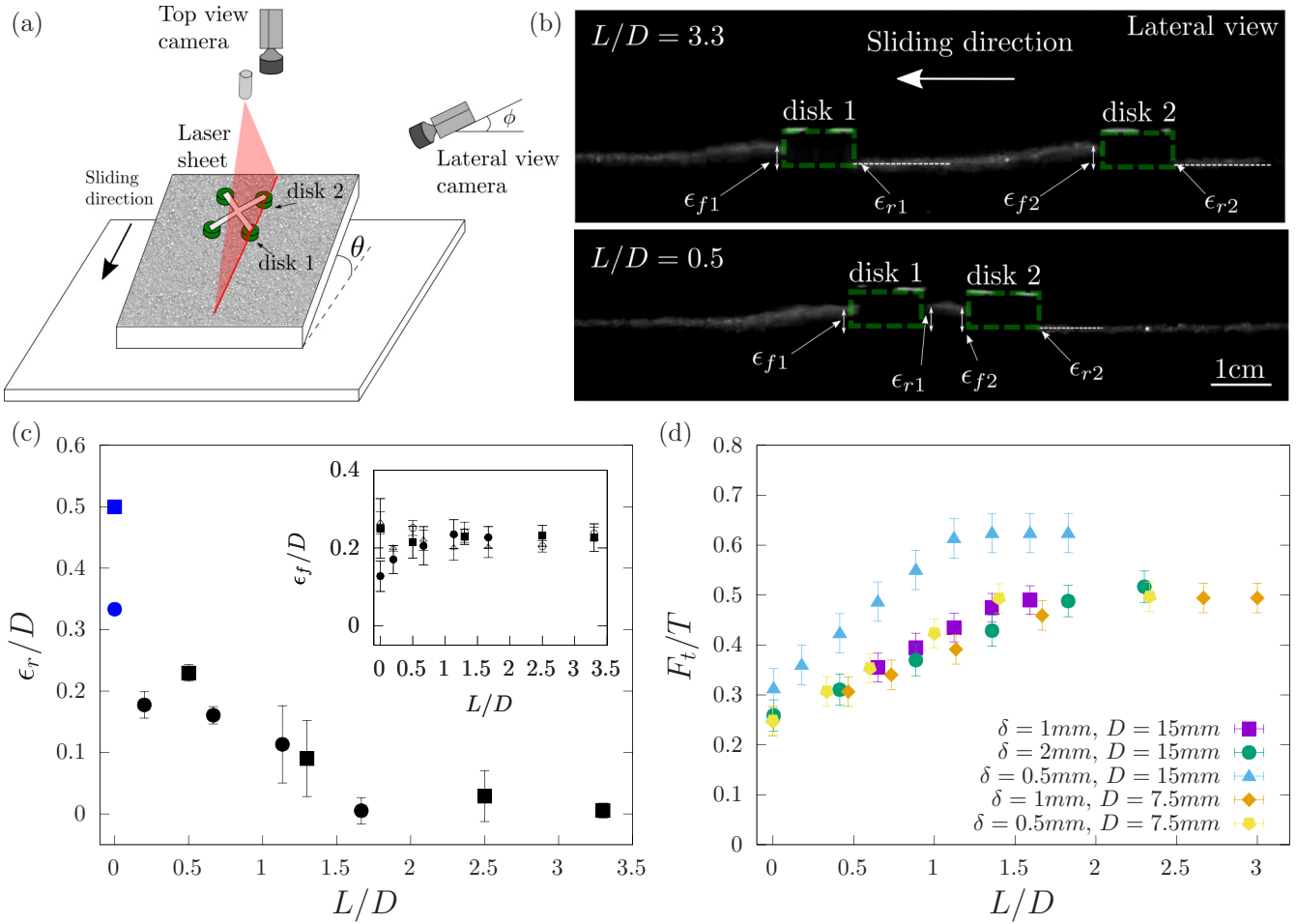


FIG. 6. (a) Schema of the experimental setup. (b) Lateral views of the artificial slider deforming the granular surface. The normalized distance between the disks is $L/D = 3.3$ (upper image) and 0.5 (bottom image). (c) Evolution of the rear rim height of the leading disk (disk 1) as a function of the nondimensional distance L/D . The blue points in the plot represent the normalized height of the leading disk edge. The inset shows the frontal rim heights of the leading and trailing disks (ϵ_{f1} : solid points; ϵ_{f2} : empty points) as a function of L/D . (d) Nondimensional force F_t/T as a function of L/D [defined in Eq. (3)]. The point codes for the different experimental parameters are the same as those in Fig. 2.

four independent rims form at each one of the disks, doubling the total force to $F_t = 4f_r$. However, the evolution of the rim force between these two extreme cases is not trivial. In an attempt to shed some light on this question, we carried out a set of experiments and measured the evolution of the frontal and rear rim heights ϵ_f and ϵ_r , respectively, as a function of L [see Fig. 6(a)]. For this, we used two artificial sliders with disk diameters $D = 10$ and $D = 15$ mm on a grain bed of $\delta = 0.5$ mm and constant pressure $P^* = 2.5$. The interdisk distance L was varied in the range $0 < L/D < 3.5$. The substrate deformation was measured using the same laser profilometry technique used in the ϵ_f vs P experiments. The pictures of the deformed surface presented in Fig. 6(b) show that, for high interdisk distance values (e.g., $L/D = 3.3$), the rims generated by the leading and trailing disks (defined in the sense of the sliding direction as disk 1 and disk 2, respectively) are almost identical. As the interdisk distance is reduced (e.g., $L/D = 0.5$), the extent of the frontal rim generated by the trailing disk (disk 2) starts to be limited by the leading disk (disk 1). A signature of this interaction may be recognized through the evolution of the rear rim depth of the leading disk ϵ_{r1} . Results presented in Fig. 6(c) show that the rear

rim height ϵ_{r1} increases as the frontal rim of the trailing disk starts to interact with the leading disk for a typical interdisk distance of $L \lesssim 1.5D = \lambda_f$ [with λ_f being estimated through the regression coefficients presented in Fig. 3(d)]. In contrast, the heights of the frontal rims of the leading and trailing disks are slightly modified when $L \rightarrow 0$ with no particular trend, and tend to quickly stabilize as L increases. The latter suggests that the height of the frontal rim is barely affected by the lateral distance between disks (in the direction perpendicular to the sliding). Still, the profile measurements being performed exclusively in the slope direction do not allow us to verify this.

D. Total force

In the particular case of the four-legged slider used in our experiments, the total rim force may be estimated as the sum of the forces acting on the four disks: two leading disks and two trailing disks. Based on the results presented before, we assume that the force acting on the two leading disks does not change as a function of the interdisk distance and may be defined as $f_{\text{lead}} = 2f_r$, where f_r is the force defined in Eq. (1).

Trying to estimate the force on the trailing disks using the same method is not straightforward, mainly due to the fact that the rear edge of the leading disk cuts the wedge generated by the trailing disk as L decreases under a certain threshold.

For the sake of simplicity, here we assume that, for L in the range $0 < L < \lambda_f$, the volume of grains displaced in front of the trailing disks is $V \sim DL(\epsilon_{f2} + \epsilon_{r1})/2$, and so the total rim force acting on the trailing disks can be expressed as

$$f_{\text{trail}} = \begin{cases} 2f_r L/\lambda_f & \text{for } L \leq \lambda_f, \\ 2f_r & \text{otherwise.} \end{cases} \quad (2)$$

The total force acting on the artificial slider F_t is equal to the sum of the forces acting on the two leading disks (f_{lead}) and the two trailing disks (f_{trail}). Assuming $\epsilon_{f1} \simeq \epsilon_{f2} = \epsilon_f$, normalization of F_t with respect to the tangential component of the slider's weight T gives

$$F_t/T = \begin{cases} \frac{f(\mu, \zeta) \hat{\epsilon}_f^2 [1+L/\lambda_f]}{\pi \hat{P} \tan \theta}, & \text{for } L \leq \lambda_f, \\ \frac{2f(\mu, \zeta) \hat{\epsilon}_f^2}{\pi \hat{P} \tan \theta}, & \text{otherwise,} \end{cases} \quad (3)$$

with $\hat{P} = P/\rho g D$ and $\hat{\epsilon}_f = \epsilon_f/D$. Figure 6(d) shows an estimation of the evolution of F_t/T as a function of the normalized interdisk distance L/D for the sliding probability experiments shown in Fig. 2. To calculate the total force the values of ϵ_f were obtained using the regression coefficients presented in Fig. 4(e). Figure 6(d) shows that despite the underestimation of the substrate forces (all cases lie below the stop condition $F_t/T \geq 1$), our model fairly captures the influence of the perturbation interactions on the global stability of our sliders on a granular incline. The trend observed for the force estimations presented in Fig. 6(d) corresponds to the slipping probability curves in Fig. 2. As the interdisk distance decreases below the threshold $L/D \lesssim 1.5$, the total force exerted by the substrate on the slider starts to decrease, followed by an increase in sliding probability.

IV. DISCUSSION

Our results point out the importance of substrate-mediated interactions on the stability of a multilegged artificial slider on a granular incline. These interactions are driven by the extent of the perturbation zones around the points of application of pressure on the granular surface. As seen through our experimental results, the substrate inclination makes perturbations generated in the front of the object (in the direction down the slope) determinant. Based on the agreement between the Coulomb method of wedges theory and our experimental observations, the extent of the frontal perturbation may be approximated as $\lambda_f \sim \epsilon_f / \tan \alpha_{\text{min}}$. The role of pressure in the evolution of λ_f is then evident, as it plays an essential role in determining the intrusion depth ϵ_f . So, for a given disk contact area, heavier sliders generate bigger perturbation zones around the contact zones. An important aspect is also the role played by the substrate inclination on stability. Figure 7 shows that the evolution of the slipping plane inclination drastically decreases as the inclination angle approaches the avalanche angle. The perturbation extent is expected to grow with plane inclination, promoting the interaction between pressure points. In this work we did not explore the

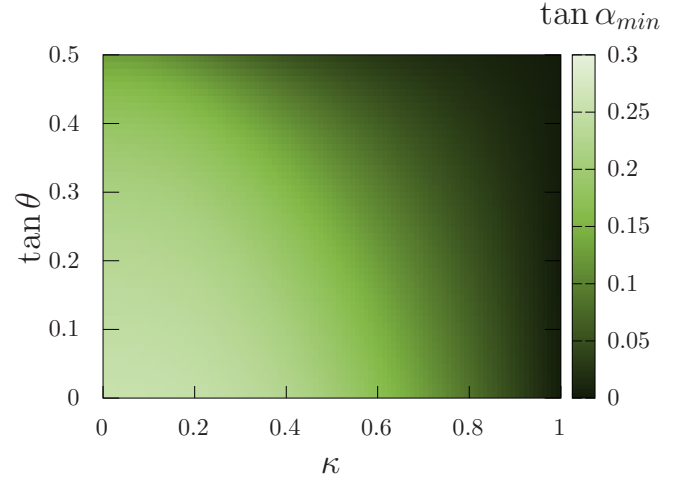


FIG. 7. Evolution of the slip plane angle α minimizing the rim force [Eq. (1)], as a function of the substrate inclination angle θ and the penetration proportion κ for an avalanche angle of $\theta_a = 28^\circ$.

dependency of λ_f on substrate inclination but it should indeed be studied in further studies. Our force model fairly captures the impact of the interdisk distance on the total force exerted by the rims on the artificial slider. The force remains constant as long as $L > \lambda_f$ and then starts to monotonically decrease down to one-half of its original value as $L \rightarrow 0$. This force loss can be crucial near the stable-unstable transition on a granular incline. This is verified by the qualitative agreement between our sliding probability experiments and our force model. Our model only includes the rim force exerted on the slider, neglecting friction between the bottom of the disks and the granular material. A full model of the substrate force should indeed include the friction force, which will need additional experimental force measurements. Nevertheless, the absence of the friction force in the model presented here does not affect the aim our work, as it should be independent of the distance between disks.

The previous results are relevant in understanding locomotion on granular media and, more precisely, in the case of granular inclines so commonly encountered by animals in nature. We have shown through model experiments that the interactions between contact zones on inclined granular media can markedly affect stability. For the four-legged slider used in our experiments, the pressure threshold defining stability can be affected by a factor of 2, depending on the interdisk distance. In the case of insects (six legs), for example, the pressure threshold may be affected up to a factor of 3, depending on the distance between tarsi in contact with the granular surface.

Different from our experiments, where the artificial walker parameters were tuned in order to keep a constant pressure on the substrate, the physical characteristics of living creatures are closely related through allometric relationships [21]. Whilst for mammals (in the range of ~ 30 g up to ~ 100 kg) isometry prevails (typical length scales as body mass to the power 1/3), negative and positive allometries can often be found in the case of insects [22–24]. Recent studies have shown how allometry may impact locomotion patterns in

walking arthropods [25]. Our results suggest that positive leg length versus mass allometries would be advantageous for locomotion on granular inclines. Indeed, as it was shown in our experiments, longer legs for a given body weight (higher values of L/λ) would enhance stability by avoiding the interaction of the perturbed regions around the leg contact points. In the case of ant locomotion on granular inclines, previous works have pointed out the importance of the ant's mass in the probability of escaping out from the antlion's pit [10,26]. In their study about ant locomotion on artificial granular inclines, Botz and collaborators [26] reported higher falling occurrences for heavier ants (*Camponotus*) than for lighter ants (*Tapinoma sessile*). The authors also observed the influence of the grain size on the falling occurrences, which appeared to be higher for small-sized grains. Even though no explicit information about the specimen's leg length is given in their work, some general information about the allometry of these two species' subfamilies can be found in Kaspari's and Weiser's work [22] on the grain size hypothesis. For the *Formicinae* subfamily (to which *Camponotus* belongs), they found a negative allometry between the ant's leg length and the ant's weight: leg length proportional to mass to the power 0.21. In contrast, for the *Dolichoderinae* subfamily (to which *Topinoma sessile* belongs), a positive allometry is reported: leg length proportional to mass to the power 0.56 (this last result is, however, not statistically significant due to the low number of measured specimens). In a more recent work, Humeau *et al.* [10] explored the capture probability of ants falling into an antlion's pit as a function of the ant mass. They found that the capture probability exhibits a maximum for intermediate weights, supporting the idea of the pressure-dependent stability discussed in Ref. [14]. In Humeau *et al.*'s work [10], the ant mass range varies from 0.5 to 10 mg and includes five different ant species. Interestingly, the species that showed the lower capture probability was *Topinoma erratum*, from the *Dolichoderinae* subfamily (positive allometry), while the species with the higher capture probability (*Lasius brunneus*) belongs to the *Formicinae* subfamily, which presents a negative allometry. However, the heaviest species (*Formica polyctena* also from the *Formicinae* subfamily) again presented low capture ratios. In the middle-weight species, Humeau *et al.* [10] also report capture probabilities for *Aphaenogaster subterranea* from the *Myrmicinae* subfamily, which, following Ref. [22], also present positive allometries, and *Lasius emarginatus* from the *Formicinae* family (negative allometry). Both species present similar mean weights: 1.85 mg for *L. emarginatus* and 1.81 mg for *A. subterranea*, but different capture rates: 51% for *L. emarginatus* ($N = 135$) and 45% for *A. subterranea*. This difference is, however, not statistically significant ($\chi^2_{(1)} = 1.08$, $p = 0.29$). The latter suggests that leg length to weight relations may be another useful clue in understanding the success of some species in walking up granular inclines. However, more

precise experiments with detailed measurements of mass and leg length, as well as on substrate penetration by the tarsi, should be done in order to confirm this hypothesis.

Although object interactions in granular media is a field that has been vastly studied in recent years [27–30], the interaction of pressure points at the surface of granular inclined planes remains unexplored. Further studies on this subject should include the dynamics of locomotion. Indeed, the rim formation and interaction strongly depends on the dynamics of the interaction between the legs and the granular media. In our experiments, for example, the artificial walker systematically slid through a typical distance of order $\sim D$ before reaching stability. Rims are not formed immediately after deposition on the granular surface but after these short slides, mainly due to the plane inclination as can be seen in Fig. 4(b) for the depth measurements. We observe that before complete arrest, heavy objects ($P^* = 5.4$) slide through a distance of $\sim 2.5D$ before the frontal rim's height is enough to stop the object. After a complete stop, inertial effects generate a slight reduction of the rim height as can be seen on the rim height's time evolution [empty squares in Fig. 4(b)]. In contrast, light objects ($P^* = 1.3$) develop a frontal rim whose height is insufficient to avoid sliding. In the latter case, the object continues sliding down the slope at constant speed with a frontal rim of constant height.

V. CONCLUSIONS

We have shown through experiments the importance of substrate-mediated interactions on the stability of a multilegged slider on a granular incline. The perturbation extent generated around each contact depends mainly on the applied pressure. For inclined granular surfaces like the one studied here, the perturbation zones are not symmetric and tend to be larger in the direction of the slope. Our experiments, as well as a physical model based on the Coulomb method of wedges, show that the total force exerted by the substrate on the walker's "legs" decreases when the interleg distance L is lower than the characteristic perturbation length λ_f . This force reduction agrees with the global stability of the walker on the incline, as shown in our sliding probability experiments where we observe an increase of the sliding probability as the interleg distance L decreases. These results are of high relevance to the global stability as well as to the locomotion efficiency of multilegged organisms and robots on granular inclines.

ACKNOWLEDGMENTS

The authors thank Jérôme Crassous for fruitful discussions and Victor Romero and Nuno from Fabriqu' Tampons Tours for their help in the fabrication of the artificial sliders.

[1] A. Hosoi and D. I. Goldman, Beneath our feet: Strategies for locomotion in granular media, *Annu. Rev. Fluid Mech.* **47**, 431 (2015).

[2] C. Li, T. Zhang, and D. I. Goldman, A terradynamics of legged locomotion on granular media, *Science* **339**, 1408 (2013).

- [3] S. Agarwal, D. I. Goldman, and K. Kamrin, Mechanistic framework for reduced-order models in soft materials: Application to three-dimensional granular intrusion, *Proc. Natl. Acad. Sci. USA* **120**, e2214017120 (2023).
- [4] B. Andreotti, Y. Forterre, and O. Pouliquen, *Granular Media: Between Fluid and Solid* (Cambridge University, Cambridge, England, 2013).
- [5] A. Fertin and J. Casas, Efficiency of antlion trap construction, *J. Exp. Biol.* **209**, 3510 (2006).
- [6] N. R. Franks, A. Worley, M. Falkenberg, A. B. Sendova-Franks, and K. Christensen, Digging the optimum pit: Antlions, spirals and spontaneous stratification, *Proc. R. Soc., Ser. B* **286**, 20190365 (2019).
- [7] D. Devetak, J. Podlesnik, I. Scharf, and T. Klenovšek, Fine sand particles enable antlions to build pitfall traps with advanced three-dimensional geometry, *J. Exp. Biol.* **223**, jeb224626 (2020).
- [8] W. M. Wheeler, *Demons of the Dust*, 1st ed. (Norton & Co., Inc., New York, 1930), p. 378.
- [9] V. Klokočovník and D. Devetak, Efficiency of antlion trap design and larval behavior in capture success, *Behav. Ecol.* **33**, 184 (2021).
- [10] A. Humeau, J. Rouge, and J. J. Casas, Optimal range of prey size for antlions, *Ecol. Entomol.* **40**, 776 (2015).
- [11] A. Humeau, M. Piñeirua, J. Crassous, and J. Casas, Locomotion of ants walking up slippery slopes of granular materials, *Integr. Organismal Biol.* **1**, obz020 (2019).
- [12] C. Li, P. B. Umbanhowar, H. Komsuoglu, D. E. Koditschek, and D. I. Goldman, Sensitive dependence of the motion of a legged robot on granular media, *Proc. Natl. Acad. Sci. USA* **106**, 3029 (2009).
- [13] N. Mazouchova, N. Gravish, A. Savu, and D. I. Goldman, Utilization of granular solidification during terrestrial locomotion of hatchling sea turtles, *Biol. Lett.* **6**, 398 (2010).
- [14] J. Crassous, A. Humeau, S. Boury, and J. Casas, Pressure-Dependent Friction on Granular Slopes Close to Avalanche, *Phys. Rev. Lett.* **119**, 058003 (2017).
- [15] A. Seguin, Y. Bertho, F. Martinez, J. Crassous, and P. Gondret, Experimental velocity fields and forces for a cylinder penetrating into a granular medium, *Phys. Rev. E* **87**, 012201 (2013).
- [16] J. S. Uehara, M. A. Ambroso, R. P. Ojha, and D. J. Durian, Low-Speed Impact Craters in Loose Granular Media, *Phys. Rev. Lett.* **90**, 194301 (2003).
- [17] W. Kang, Y. Feng, C.-S. Liu, and R. Blumenfeld, Archimedes' law explains penetration of solids into granular media, *Nat. Commun.* **9**, 1101 (2018).
- [18] R. M. Nedderman, *Statics and Kinematics of Granular Materials* (Cambridge University, Cambridge, England, 1992).
- [19] H. Guo, J. Goldsmith, I. Delacruz, M. Tao, Y. Luo, and S. A. Koehler, Semi-infinite plates dragged through granular beds, *J. Stat. Mech.* (2012) P07013.
- [20] B. Percier, S. Manneville, J. N. McElwaine, S. W. Morris, and N. Taberlet, Lift and drag forces on an inclined plow moving over a granular surface, *Phys. Rev. E* **84**, 051302 (2011).
- [21] J. T. Bonner, *Why Size Matters: From Bacteria to Blue Whales* (Princeton University, Princeton, NJ, 2006).
- [22] M. Kaspari and M. D. Weiser, The size–grain hypothesis and interspecific scaling in ants, *Funct. Ecol.* **13**, 530 (1999).
- [23] M. Kaspari and M. Weiser, The size–grain hypothesis: do macroarthropods see a fractal world?, *Ecol. Entomol.* **32**, 279 (2007).
- [24] M. Teuscher, M. Brandle, V. Traxel, and R. Brandl, Allometry between leg and body length of insects: Lack of support for the size–grain hypothesis, *Ecol. Entomol.* **34**, 718 (2009).
- [25] J. Tross, H. Wolf, and S. E. Pfeffer, Allometry in desert ant locomotion (*Cataglyphis albicans* and *Cataglyphis bicolor*)—does body size matter?, *J. Exp. Biol.* **224**, jeb242842 (2021).
- [26] J. T. Botz, C. Loudon, J. B. Barger, J. S. Olafsen, and D. W. Steeples, Effects of slope and particle size on ant locomotion: Implications for choice of substrate by antlions, *J. Kansas Entomol. Soc.* **76**, 426 (2003).
- [27] F. Pacheco-Vázquez and J. C. Ruiz-Suárez, Cooperative dynamics in the penetration of a group of intruders in a granular medium, *Nat. Commun.* **1**, 123 (2010).
- [28] A. Merceron, A. Sauret, and P. Jop, Cooperative effects induced by intruders evolving through a granular medium, *Europhys. Lett.* **121**, 34005 (2018).
- [29] M. Dhiman, S. Kumar, K. Anki Reddy, and R. Gupta, Origin of the long-ranged attraction or repulsion between intruders in a confined granular medium, *J. Fluid Mech.* **886**, A23 (2020).
- [30] V. L. Díaz-Melián, A. Serrano-Muñoz, M. Espinosa, L. Alonso-Llanes, G. Viera-López, and E. Altshuler, Rolling away from the Wall into Granular Matter, *Phys. Rev. Lett.* **125**, 078002 (2020).